NAVAL POSTGRADUATE SCHOOL

MONTEREY, CALIFORNIA

THESIS

CHARACTERISTICS OF SUMMERTIME MARINE FOG OBSERVED FROM A SMALL REMOTE ISLAND

by

Kelsey M. Rowe

June 2023

Thesis Advisor: Qing Wang
Co-Advisor: Jesus Ruiz-Plancarte

Approved for public release. Distribution is unlimited.

THIS PAGE INTENTIONALLY LEFT BLANK

REPORT DOCUMENTATION PAGE		*Form Approved OMB No. 0704-0188*

Public reporting burden for this collection of information is estimated to average 1 hour per response, including the time for reviewing instruction, searching existing data sources, gathering and maintaining the data needed, and completing and reviewing the collection of information. Send comments regarding this burden estimate or any other aspect of this collection of information, including suggestions for reducing this burden, to Washington headquarters Services, Directorate for Information Operations and Reports, 1215 Jefferson Davis Highway, Suite 1204, Arlington, VA 22202-4302, and to the Office of Management and Budget, Paperwork Reduction Project (0704-0188) Washington, DC 20503.

1. AGENCY USE ONLY *(Leave blank)*	2. REPORT DATE June 2023	3. REPORT TYPE AND DATES COVERED Master's thesis
4. TITLE AND SUBTITLE CHARACTERISTICS OF SUMMERTIME MARINE FOG OBSERVED FROM A SMALL REMOTE ISLAND		**5. FUNDING NUMBERS**
6. AUTHOR(S) Kelsey M. Rowe		
7. PERFORMING ORGANIZATION NAME(S) AND ADDRESS(ES) Naval Postgraduate School Monterey, CA 93943-5000		**8. PERFORMING ORGANIZATION REPORT NUMBER**
9. SPONSORING / MONITORING AGENCY NAME(S) AND ADDRESS(ES) N/A		**10. SPONSORING / MONITORING AGENCY REPORT NUMBER**
11. SUPPLEMENTARY NOTES The views expressed in this thesis are those of the author and do not reflect the official policy or position of the Department of Defense or the U.S. Government.		
12a. DISTRIBUTION / AVAILABILITY STATEMENT Approved for public release. Distribution is unlimited.		**12b. DISTRIBUTION CODE** A

13. ABSTRACT (maximum 200 words)

This research is part of the Fog and Turbulence Interactions in the Marine Atmosphere (FATIMA) project focusing on the physical processes in marine fog and their impact on optical attenuation. This observational study is based on the measurements from Sable Island during the FATIMA Grand Banks field campaign. The analyses used the water droplet size distribution from a fog monitor (FM-120) and the meteorological optical range (MOR) measured by a present weather sensor (PWD22) as the main data source augmented by frequent radiosonde launches. Based on the 35 days of measurements, we identified nine reduced visibility events (RVEs). The radiosonde profiles revealed the complex layered thermodynamic structure within and above the fog layers and the frequent presence of high surface winds up to 16 ms-1 and a low-level jet, while the droplet spectra indicated a bimodal distribution below droplet size of 50 μm for most RVEs. Although the complete dataset under all weather conditions follows the same general trend of increasing MOR with decreasing liquid water content (LWC), the heavy fog events (visibility below 400 m) show different rates of decrease. We also found that representing both fog and mist using a single power function was unrealistic. Furthermore, the empirical relationship is sensitive to the length of averaging. Therefore, empirical functions derived from the nominal 1-min data may not be suitable for mesoscale models with a much coarser temporal output of LWC.

14. SUBJECT TERMS coastal fog, fog microphysics, optical attenuation, visibility, fog optical properties, liquid water content			**15. NUMBER OF PAGES** 55
			16. PRICE CODE
17. SECURITY CLASSIFICATION OF REPORT Unclassified	**18. SECURITY CLASSIFICATION OF THIS PAGE** Unclassified	**19. SECURITY CLASSIFICATION OF ABSTRACT** Unclassified	**20. LIMITATION OF ABSTRACT** UU

NSN 7540-01-280-5500

Standard Form 298 (Rev. 2-89)
 Prescribed by ANSI Std. 239-18

THIS PAGE INTENTIONALLY LEFT BLANK

**CHARACTERISTICS OF SUMMERTIME MARINE FOG
OBSERVED FROM A SMALL REMOTE ISLAND**

Kelsey M. Rowe
Lieutenant Commander, United States Navy
BS, United States Naval Academy, 2013

Submitted in partial fulfillment of the
requirements for the degree of

**MASTER OF SCIENCE IN METEOROLOGY AND PHYSICAL
OCEANOGRAPHY**

from the

**NAVAL POSTGRADUATE SCHOOL
June 2023**

Approved by: Qing Wang
                Advisor

                Jesus Ruiz-Plancarte
                Co-Advisor

                Wendell A. Nuss
                Chair, Department of Meteorology

iii

THIS PAGE INTENTIONALLY LEFT BLANK

ABSTRACT

This research is part of the Fog and Turbulence Interactions in the Marine Atmosphere (FATIMA) project focusing on the physical processes in marine fog and their impact on optical attenuation. This observational study is based on the measurements from Sable Island during the FATIMA Grand Banks field campaign. The analyses used the water droplet size distribution from a fog monitor (FM-120) and the meteorological optical range (MOR) measured by a present weather sensor (PWD22) as the main data source augmented by frequent radiosonde launches. Based on the 35 days of measurements, we identified nine reduced visibility events (RVEs). The radiosonde profiles revealed the complex layered thermodynamic structure within and above the fog layers and the frequent presence of high surface winds up to 16 ms-1 and a low-level jet, while the droplet spectra indicated a bimodal distribution below droplet size of 50 μm for most RVEs. Although the complete dataset under all weather conditions follows the same general trend of increasing MOR with decreasing liquid water content (LWC), the heavy fog events (visibility below 400 m) show different rates of decrease. We also found that representing both fog and mist using a single power function was unrealistic. Furthermore, the empirical relationship is sensitive to the length of averaging. Therefore, empirical functions derived from the nominal 1-min data may not be suitable for mesoscale models with a much coarser temporal output of LWC.

THIS PAGE INTENTIONALLY LEFT BLANK

TABLE OF CONTENTS

THIS PAGE INTENTIONALLY LEFT BLANK

LIST OF FIGURES

THIS PAGE INTENTIONALLY LEFT BLANK

LIST OF TABLES

THIS PAGE INTENTIONALLY LEFT BLANK

LIST OF ACRONYMS AND ABBREVIATIONS

CCN   cloud condensation nuclei

CDP   Cloud Droplet Probe

DMT   Droplet Measurement Technologies

ED   effective droplet diameter

EO   electro-optical

FATIMA   Fog and Turbulence Interactions in the Marine Atmosphere

FM   fog monitor

FSO   free-space optical

HEL   high-energy laser

IR   infrared

LWC   liquid water content

MOR   meteorological optical range

MVD   mean volume diameter

N_d total droplet number concentration

NWP   numerical weather prediction

PWD   present weather detector

q_l liquid water content

Q_{sct} scattering efficiency

R_e droplet effective radius

R_m mean droplet radius

RVE   reduced visibility events

SYNOP   synoptic

WMO   World Meteorological Organization

σ_a volume absorption coefficient

σ_e volume extinction coefficient

σ_s volume scattering coefficient

THIS PAGE INTENTIONALLY LEFT BLANK

ACKNOWLEDGMENTS

THIS PAGE INTENTIONALLY LEFT BLANK

I.   INTRODUCTION

A.   CONTEXT

Fog is suspended water or ice droplets in the lower atmosphere with near-ground visibility of less than 1 km. Fog evolution is governed by numerous dynamic and thermodynamic, microphysical, and physicochemical processes from microscale to synoptic scale. The interactions of these processes are critical in determining the physical properties of fog. These contributing factors and the significant temporal and spatial variability make accurate marine fog forecasts a significant challenge. Furthermore, current numerical weather prediction (NWP) models typically have grid resolution between 1 to 10 km. In these types of models, it is impossible to reduce grid spacing to the sizes of cloud/fog droplets to resolve the fine-scale processes. However, these small-scale processes play an important role in fog evolution (Gultepe et al. 2006). Therefore, many of the physical processes within fog have to be parameterized in terms of grid-scale predictive quantities to statistically represent the evolution of particle populations (Morrison et al. 2020), making the accurate forecast of the life cycle of a fog layer an extremely challenging task (Stoelinga and Warner 1999; Bergot 2013; Koračin et al. 2001). A better understanding of the characteristics of a broad spectrum of fog events is needed. Still, it has been difficult due to the large variability of fog in their composition, formation, and evolution.

B.   MILITARY APPLICATION

Fog can significantly impact military operations, affecting all warfare areas. Fundamentally accurate fog forecasts are vital for safety of navigation and flight operation. This study aims to improve fog forecasts by better depicting the relationship between fog microphysics and boundary layer physics in numerical weather prediction (NWP) models. One area of particular importance is improving our understanding of the Atmospheric Effects of fog on Optical Systems due to the increasing utilization of free-space optical (FSO) communication, EO/IR sensors, and high-energy laser (HEL) weapon systems. As a result, understanding and forecasting are paramount. Increased understanding of coastal

1

fog will enhance the exploitation of the environmental battlespace and increase lethality in an otherwise mission-limiting environment.

C.   THESIS OBJECTIVES

This study aims to gain a fundamental understanding of marine fog, focusing on the characteristics of fog microphysics and its temporal and spatial variation and quantifying the relationship between fog microphysics and their impact on optical propagation. Many past observational studies on fog were based on measurements over land surfaces or coastal regions (e.g., Koračin et al. 2001; Gultepe et al. 2006; Dupont et al. 2016; Fernando et al. 2021, Gultepe et al. 2021; Wang et al. 2021b). Few studies were made in the open ocean marine environment. This study utilizes in-situ measurements of fog events from an upwind location of a small remote island, Sable Island, about 110 miles off the coast of Nova Scotia. The data was collected as part of the FATIMA (Fog and Turbulence Interactions in the Marine Atmosphere) Grand Bank field campaign from 27 June 2022 to 31 July 2022. The entire dataset was used to examine the thermodynamic and microphysics properties of a broad range of hygrometer types observed during the field campaign and was categorized based on visibility and precipitation. The relationship between fog microphysics and optical attenuation is also explored to improve future forecast capability of visibility based on macro- and micro-fog microphysics.

In the following chapters, we first introduce the key microphysics and attenuation variables and the methodology to obtain these variables in the background and methodology section. The Fatima field campaign and the Sable Island measurements are discussed in Chapter III. Results on fog microphysics and optical attenuation are given in Chapter IV followed by a summary and conclusions.

II.   KEY PHYSICAL PARAMETERS OF MICROPHYSICS AND OPTICAL ATTENUATION

Microphysics refers to the microscale processes that affect cloud/fog/precipitation particles and is a critical connection between atmospheric water and energy cycles (Morrison et al. 2020). It describes how cloud droplets and precipitation evolve, including condensate characteristics and precipitating hydrometeors. The fundamental microphysical variables are droplet size distribution (or droplet spectrum), Liquid water content (LWC) represented by q_l, and total droplet number concentration (N_d). Droplet size can be represented by some macroscopic statistical descriptions such as the mean droplet radius (R_m), the effective droplet diameter (ED), and the mean volume diameter (*MVD*). If the radius of a fog droplet is expressed as r, with the droplet size spectra represented by *n(r)*, Equation 1 gives the relationship between the total droplet number concentration, LWC, and the effective diameter and the droplet spectra. These expressions were used to derive the various macroscopic description of the fog microphysics from the measured droplet spectra.

$$N_d = \int n(r)dr, \; ED = \frac{2\int n(r)r^3 dr}{\int n(r)r^2 dr}, \; q_l = \int \frac{4}{3}\pi\rho_\omega n(r)r^3 dr, \; MVD = \left(\frac{2\int n(r)r^3 dr}{\int n(r)dr}\right)^{\frac{1}{3}} \qquad (1)$$

The formation and evolution of fog encompasses complex interactions among aerosol number concentration, size, composition, thermodynamics, radiation, and the microphysical and dynamical processes (see a review in Gultepe et al. 2007). The droplet number concentration, N_d, is mainly controlled by the number and properties of the cloud condensation nuclei (CCN), as illustrated by many previous studies on cloud optical properties (Twomey 1977; Albrecht 1989; Gultepe 2017). Different sources of CCN, such as those from anthropogenic pollution, may change the cloud droplet size and hence affect its optical depth, termed the Twomey effect. This is true for fog which is an important factor in regulating the impact of fog on visibility (Mazoyer et al. 2019). The effective radius is also a key parameter of fog directly related to the optical property of the cloud/fog (Correia et al. 2022). In addition to Equation 1, droplet effective radius (R_e), half of the ED, can be retrieved through remote sensing of the cloud/fog layer, such as measurements

3

from the Geostationary satellites. The typical LWC of fog is between 0.01-0.4 g m^{-3} (Roach 1976). LWC is related to droplet concentration and size, as shown in equation 1 (Gerber 1981; Gerber 1991; Garcia-Garcia et al. 2002; Fuzzi et al. 1992; Jiusto 1981). Alternatively, LWC can be directly measured by bulk microphysics sensors such as the King probe, a hot-wire liquid water device that determines LWC by maintaining a cylinder/wire at a constant temperature when exposed to air and then measuring the heat released when water droplets are vaporized (King et al. 1978). A Cloud Droplet Probe (CDP) or a fog monitor such as the FM-120 used for this study are cloud/fog droplet size spectrometer that measures fog droplet spectra and reports calculated droplet statistics (Wang 2021a).

Radiative energy passing through the atmosphere is affected by absorption and scattering from molecules and suspended particles such as aerosols and hydrometers. Transmittance (τ) quantifies how much energy will make it through a given medium at a given path length. It is a function of wavelength, optical properties of the media, and the propagation path length (L).

$$\tau(\lambda, L) \ = \ \frac{E_R}{E_T} = exp\left(-\int_a^b \sigma_e \, ds\right) \qquad (2)$$

Here, the integrand is referred to as the optical depth $\delta_\lambda = \int_a^b \sigma_e \, dS = \int_a^b k(\lambda)\rho dS$). The volume extinction coefficient (m^{-1}) is the combination of the volume absorption coefficient (σ_a) and volume scattering coefficient (σ_s).

$$\sigma_e = \ \sigma_a + \sigma_s \qquad (3)$$

These coefficients are functions of the wavelength of the incident irradiance, the molecular constituents, and the physical and chemical properties of aerosols or suspended hydrometers, cloud condensation nuclei (CCN) (Wang 2021a). For optical attenuation in the visible wavelength band, the scattering coefficient is the primary contributor to the overall extinction coefficient, while the absorption impacts are negligible (Isaac 2001).

Scattering of radiance to a specific direction is a function of the viewing angle, index of refraction, and the size parameter (r/λ). Scattering in fog falls under the Mie

4

scattering regime as the scatterers, the water droplets, are similar to the wavelengths of interest.

$$\sigma_s = \int_{r1}^{r2} \pi r^2 Q_{sct}\left(mr, \frac{r}{\lambda}\right) n(r)dr \qquad (4)$$

where mr represents the real part of the refractive index, and Q_{sct} is the scattering efficiency (Petty 2004). As shown in Equation 4, Mie scattering is a strong function of size distribution and a weak function of wavelength. Therefore, it is critical to have accurate droplet size spectra when analyzing optical attenuation in fog.

Accessing visibility is the key aspect in the identification of fog. Fog-induced visibility reduction is regulated by the concentration of CCN and the resulting distribution of droplet sizes (Dorman 2017). Meteorological Optical Range (MOR) is used to represent visibility and, subsequently, the intensity of fog. The Koschmieder equation

$$m = \frac{c}{\sigma_e} \qquad (5)$$

directly links MOR, as defined by m, to the atmospheric extinction coefficient with $c = \ln\left(\frac{1}{0.05}\right) = 2.996$. Visibility can therefore represent the atmospheric attenuation of optical signals (Wang 2021a).

5

THIS PAGE INTENTIONALLY LEFT BLANK

III. DATA COLLECTION AND PROCESSING

FATIMA is a multi-university research initiative aimed at understanding the marine fog and its interaction with turbulence on various scales, from synoptic to micro-scale. Two field campaigns were planned in FATIMA, the first of which occurred offshore of Nova Scotia, referred to as FATIMA Grand Banks (Fernando et al. 2023, unpublished manuscript). Data collection at this location occurred from 27 June 2022 to 31 July 2022. In addition to measurements on a modified supply vessel, extensive measurements were made on Sable Island, sitting 109 miles offshore of Nova Scotia in the North Atlantic (Figure 1a).
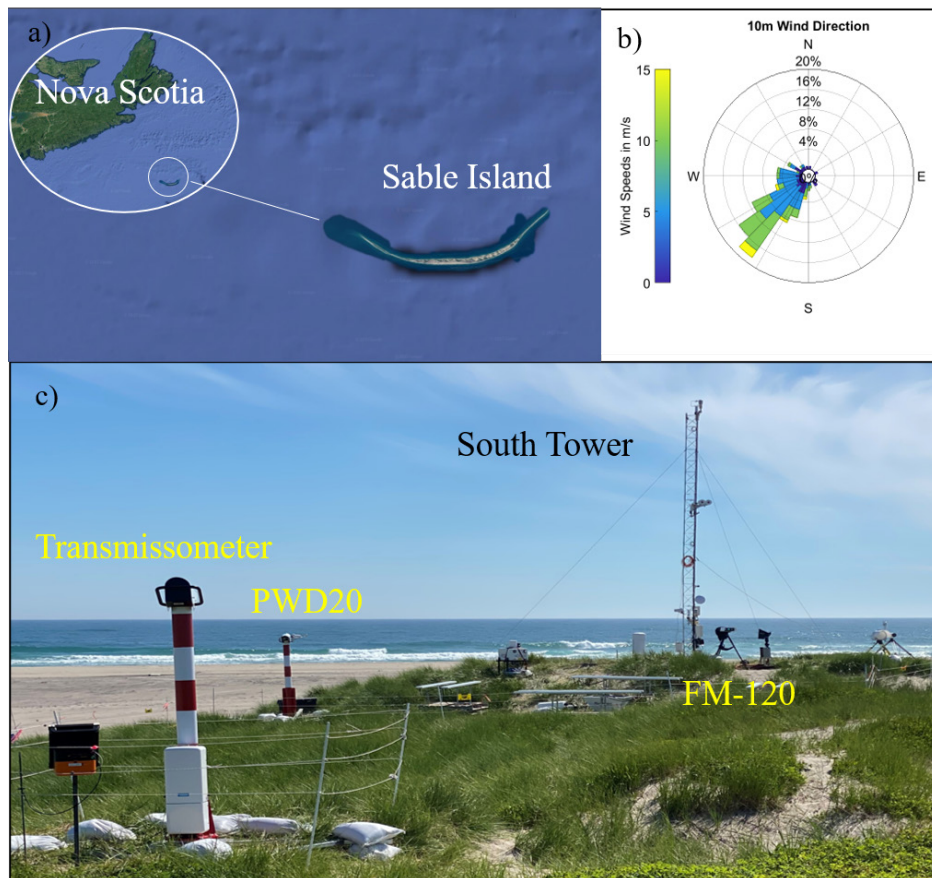
a) Google earth imagery depicting the field study location. b) 10-meter wind speed and direction during the campaign. c) South Tower equipment setup, containing a Vaisala Present Weather Detector (PWD22) and Fog Monitor (FM-120) droplet spectrometer.

Figure 1.   Sable Island field study set-up

7

Sable Island is a narrow crescent-shaped island, approximately 1km across at its widest section and 42 km on the long side. Figure 1b shows the predominant southwest wind direction during the campaign, which is consistent with climatology analyses prepared for the FATIMA Grand Banks experiment. The instrument set-up was deliberately oriented southwest in the direction parallel with the expected prevailing winds. Figure 1c shows the setup of instruments on the south end of the Sable Island measurement array where the measurements used in this research were made. The suite of sensors at this location is about 180 m to the south waterline. Given the proximity to the upwind ocean, the measurements from this site are the closest to the marine environment.

The FATIMA Sable Island site consisted of three major towers aligned along the predominant southwesterly wind direction across the narrow width of the island. Each tower was equipped to measure or calculate multi-level turbulence, thermodynamics, fog liquid water content, and visibility measurements supplemented with adjacent radiation and fog microphysics measurements. The measurements that provided the primary data for this study were made near the south tower with the least amount of land impact from the island. The main instruments include a Vaisala Present Weather Detector (PWD22) and a Droplet Measurement Technologies (DMT) Fog Monitor (FM-120). The proximity of PWD22 and FM-120 ensures that the in-situ measurements are of the same patch of fog. This is crucial to account for fog microphysics' substantial temporal and spatial variability. The FM-120 is the main instrument used in our data collection to quantify droplet size distribution. FM-120 is a cloud droplet size spectrometer that measures droplet size spectra. It is designed with a solid-state laser diode and compact electronics technology for ground or tower-based studies (Droplet Measurement Technologies, 2018). The FM-120 has a droplet diameter range of 2–50 μm. The reported value of LWC is an integrated value for that droplet size range. Visibility, or MOR, was measured by the Vaisala PWD22. The PWD22 is a multi-variable sensor that uses a forward scatter system to provide accurate estimates of MOR and uses a RAINCAP rain sensor to measure the intensity and amount of precipitation. The RAINCAP rain sensor assembly produces a signal proportional to the amount of water on the sensing element. The PWD22 is a point measurement of visibility. It takes instantaneous (15 s) visibility values that are averaged to get 1-min and 10-min

average output. The MOR was derived from the mean extinction coefficients expressed as MOR$_{fo}$(m)=3000/(σ_e [1/km]). Precipitation type and intensity are reported using NWS and World Meteorological Organization (WMO) SYNOP (synoptic) weather codes every 15 seconds. Fog is defined when visibility is lower than 1 km. While the WMO has not clearly delineated the upper visibility limit of mist, the PWD22 used the accepted standard of 10 km, leaving mist defined as visibility between 1 and 10 km. The 'clear' condition is defined as visibility higher than 10 km with no precipitation. If precipitation is present regardless of visibility, the weather code will register as precipitation (Vaisala 2004). The PWD22 is part of the Vaisala transmissometer located about 15 m east of the FM-120. Most of the time, they were seen within the same fog patch.

The upper atmosphere was probed using radiosondes (model DigiCora sounding system MW41, Vaisala, Finland) launched approximately every three hours using 50 g balloons (KCI 150, Kaymont, Melbourne, FL). The frequency of launches was determined and modified in the field based on scientific goals and existing weather conditions. The meteorological data captured included air temperature, relative humidity, atmospheric pressure, wind speed, wind direction, and GPS coordinates.

The original data have gone through extensive data quality control before our analyses. In particular, some of the FM housekeeping variables were analyzed as part of the extensive quality control process. For example, data sections with laser current out of the prescribed (50-100 mA) range or laser block temperatures outside healthy readings (20-20°C) were eliminated. Two periods (07/03/22 03:03 -09:00 and 07/04/22 04:51-10:25) of questionable data quality based on housekeeping variables and measurements were also eliminated.

THIS PAGE INTENTIONALLY LEFT BLANK

IV. RESULTS

This section is divided into two components. We will first discuss fog microphysics and relevant boundary layer thermodynamics. An investigation into the impacts of the microphysical parameters on optical attenuation will follow in the next subsection.

## A. THERMODYNAMICS, FOG CONDITIONS AND MICROPHYSICS

A total of 177 radiosondes were launched from Sable Island during the FATIMA 2022 Grand Banks campaign to provide insight into the prevailing meteorological conditions during the time of the study as well as detailed profiles that show the evolution of the lower atmospheric structure and fog layers. Figure 2 gives the time-height plot of four variables of main concern, including potential temperature, relative humidity, wind speed, and wind direction. When a sounding went through a fog layer, the top of the fog layer is identified by the height above which the air becomes unsaturated (relative humidity < 100%). Fog layer tops are also shown in Figure 3. Generally, there was a shallow cool layer of atmosphere near the surface nominally below about 200 m based on the potential temperature plot (Figure 2a). The main capping inversion varied in heights between 1 and 2.5 km above the surface during the early part of the field campaign and significantly lowered between 18 and 27 July. The relative humidity profile does not resemble that of potential temperature, except for the lowest levels, where saturated layers above nominally 200 m and below ~1.5 km usually have the observed fog layer from the surface-based FM-120. Figure 2c also revealed the frequent occurrence of high wind conditions exceeding 10 ms^{-1} close to the surface with a maximum of up to 16 m s^{-1}. Interestingly, fog was detected frequently under high wind conditions on Sable Island, starkly contrasting previously observed radiation fog overland (Price 2019). Figure 2 also shows that the high wind events were often accompanied by moist air above the cool, moist near-surface fog layer. Winds were predominately southwesterly and westerly as expected (Figures 1b and 2d).
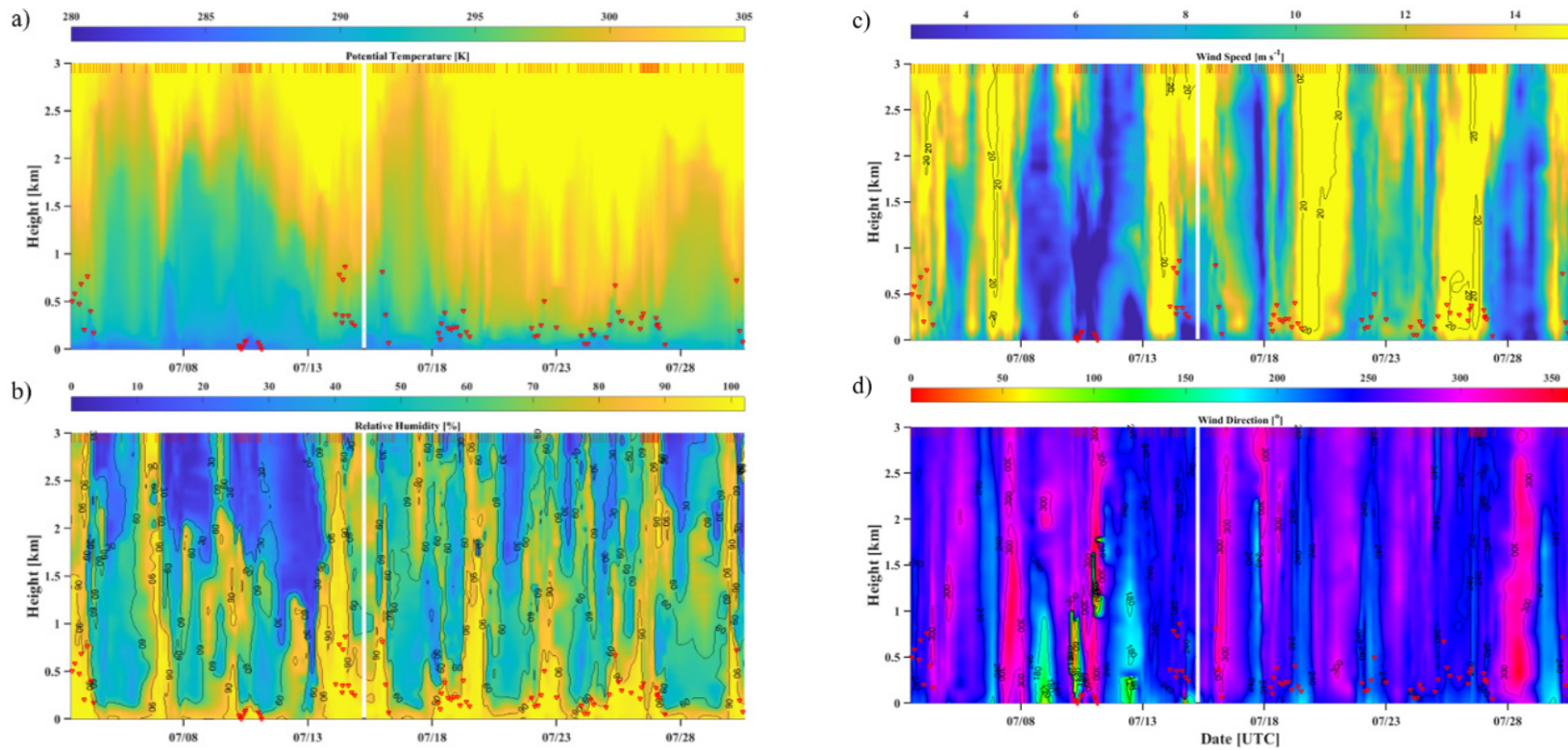
Radiosonde soundings of a) potential temperature, b) relative humidity, c) wind speed, d) wind direction. The magenta dotted lines at the top of each figure delineate the time of each radiosonde launch. The red downward triangles denote the fog layer top, as identified from the analysis of individual soundings.

Figure 2.   Radiosonde soundings

12

To illustrate the vertical variability of thermodynamics and wind associated with the fog layer, we focused on four sounding profile plots selected out of the 177 soundings in Figure 3. These four soundings are representative of the most-observed profiles. Figures 3a, c, and d all show the presence of a fog layer in the presence of a low-level jet with maximum wind speed at ~400 m above the surface. Figure 3a and c also shows directional shear. In the case of Figure 3a, the jet maximum (the nose) is within the fog layer, while in Figures 3c and d, the jet sat above the fog layer of ~200 m and 380 m in depth, respectively. Thermal stratification also varies in these soundings, with a general trend of stable stratification in the fog layer. Figure 3b shows a well-defined fully-mixed fog layer up to 120 m with a capping inversion and sharp moisture lapse in the inversion, a vertical structure closely resembles those in the stratocumulus-topped boundary layers (e.g., Wang and Albrecht 1994). Figure 3a shows a stably stratified fog layer extending to the top of the fog layer, although the lowest 100 m or so had much stronger stratification than the layer above, where RH was close to 100%. In Figure 3c, although the saturated fog layer is up to ~200 m, there is clearly a moist layer above extending to the top of the low-level jet. This sounding profile indicates mixing as a result of the vertical wind shear associated with the low-level jet, although the warm layer above the fog layer kept the layer from saturation. These layered structures in temperature, moisture, and wind illustrate the complex interaction among the various physical processes controlling the marine boundary layer and the fog layer involving buoyancy and shear-generated turbulent mixing and perhaps infrared radiative cooling as in stratocumulus clouds. Furthermore, in Figure 3d, a thin unstable layer at the surface below ~50 m is present. This very thin layer is also unsaturated with a significant drop in specific humidity. This thin layer appears frequently in the soundings, especially during midday. It is likely the impact of the land surface of the island. Note that the balloon soundings were released near the center tower about 350 m north of the southern coastline.

13
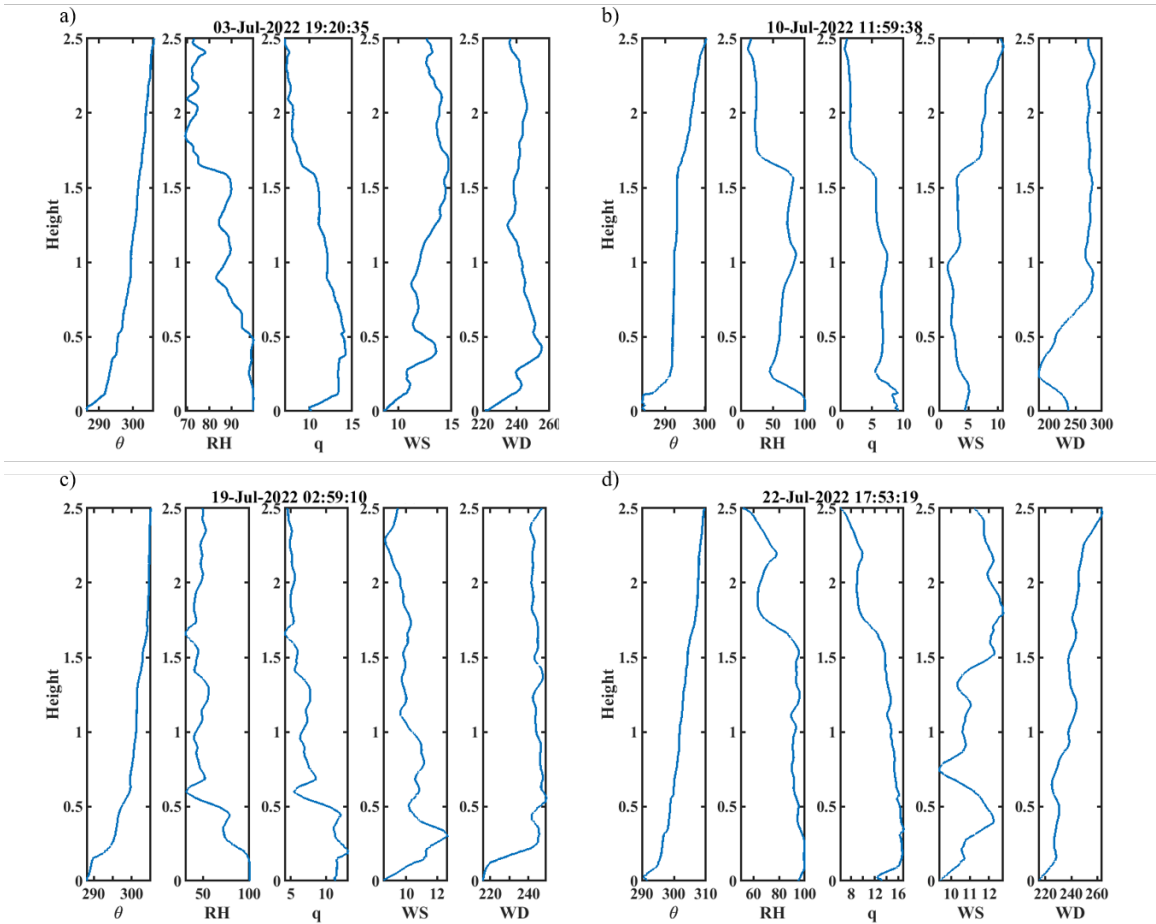
Soundings of four selected cases illustrating typical sounding profiles from Sable Island. Soundings shown were taken at a) 07/03/22 at 19:20, b) 07/10/22 at 11:59, c) 07/19/22 at 02:59 d) 07/22/22 at 17:53. Times are in UTC. Here, θ, RH, q, WS, and WD are potential temperature (Kelvin), relative humidity (%), specific humidity (g kg^{-1}), wind speed (m s^{-1}), and wind direction, respectively.

Figure 3.   Typical sounding profiles from Sable Island

Time series of various microphysical parameters, including LWC, N_d, and ED, were generated based on the FM-120 size spectra (Figure 4). For this study, all times are in UTC. During the summer, the local time on Sable Island is -3 UTC. Based on the PWD22 measurements at 1-min resolution, each measurement point can be categorized into the four types of weather code discussed earlier. Figure 5 shows the breakdown of the probability of occurrence for each weather code during the observational period. Figure 5 shows that mist has the most frequent presence at 44%, while fog occurred during 30% of the time during the observation period. Precipitation was observed 14% of the time.

14
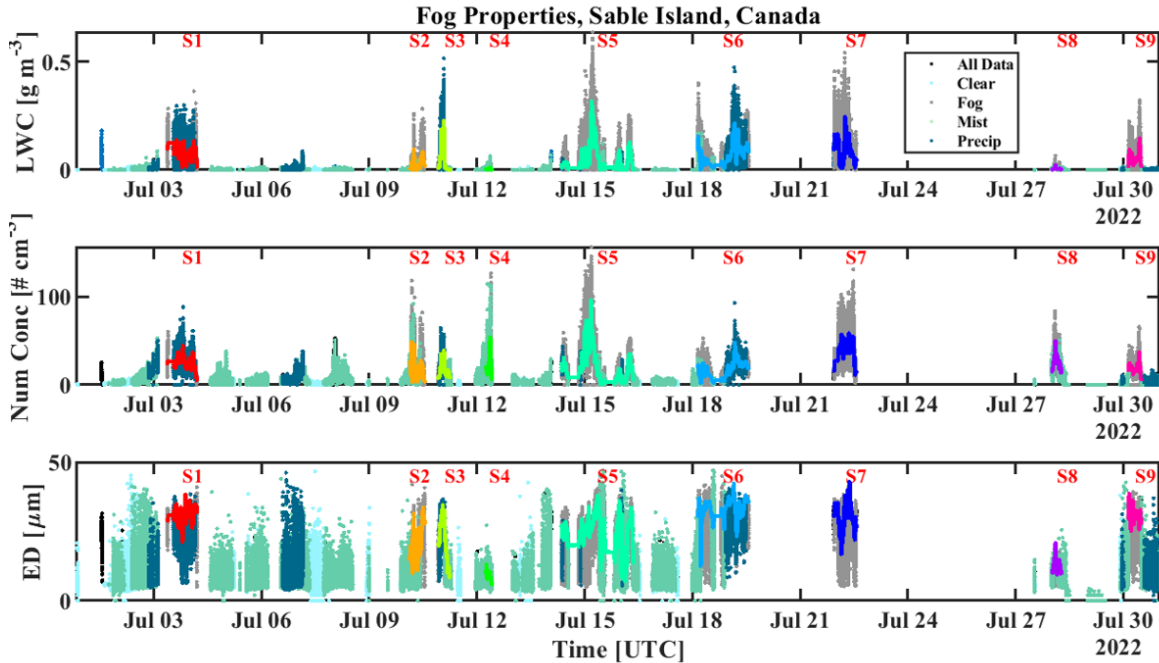
Data points are categorized and colored by WMO SYNOP codes from the PWD22. The rainbow-colored lines are the 5-minute moving average of the plotted variable during the period of interest. The events are labeled in red at the top of the figure.

Figure 4.   Time series of LWC, N_d (Num Conc), and ED from the FM-120

A total of nine periods of interest, "events," were identified as reduced visibility events for further analysis. The start and end of each fog event were determined based on visibility measurements from the PWD. Events are defined as periods of mean visibility less than 1km for more than 2 hours. If subsequent periods of visibility less than 1km were within 8 hours, they were grouped as one event. These events, referred to as S1-S9, are shown in Figure 3a using different colors to plot the corresponding 5-min mean quantity on top of the 1-min data color-coded for weather codes. The timing, duration, and mean microphysics properties of each event are detailed in Table 1. The events lasted between 4.1h (S4) and 48.03h (S5). The two most short-lived events, S4 and S8, had the smallest average droplet sizes shown in ED and MVD. S7 had the lowest MOR and highest mean LWC. Fog with LWC levels higher than the typically observed values, 0.01-0.4 g m^{-3}, were observed in four of the nine events (S3, S5, S6, and S7). The microphysics time series

(Figure 4) and the varied characteristics shown in Table 1 highlight the complexity of reduced visibility events with substantial temporal and spatial variability.
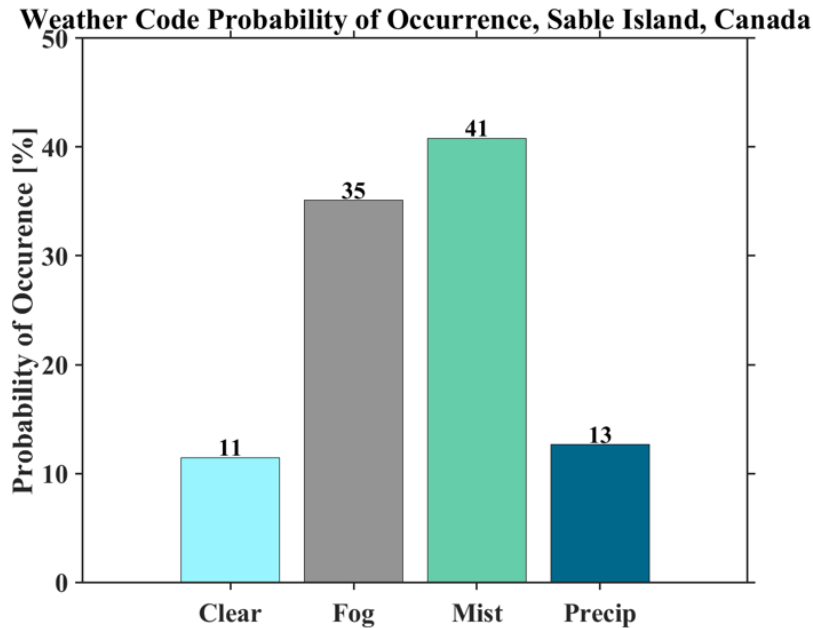

Figure 5.   Probability of occurrence of WMO SYNOP code during the field campaign

Figure 4 shows that events S1, S3, and S6 are predominantly precipitation events, while the remaining of the reduced visibility events are categorized as fog. However, since the association of weather code with visibility was based on 1-min data, none of the identified events are associated with a single weather code, as demonstrated in Figure 6. Figure 6b shows that the weather code conditions can change in a manner of minutes. Here, we see a brief period of mist at 09:48 before transitioning back to fog and then mist. Visibility increases again around 10:07 and decreases back to fog by 10:12. The mixed presence of different weather codes in any single events results from the large variability in MOR, as shown in Table 1. Here we found that the standard deviation of MOR can be the same magnitude or even larger than the measurement of MOR itself. The differences between the maximum LWC or N_d and their corresponding mean values reveal substantial variability within a single event.

16

Table 1.   Characteristics of the reduced visibility events (RVE)

Fog event	Start time (UTC)	End time (UTC)	Duration (h)	q_l (g m^{-3})	N_d (cm^{-3})	ED (μm)	MVD (μm)	MOR (km)
S1	07/03/22 0900	07/04/22 0500	20	0.364/0.079	88.4/26	26.2	31.2	0.32/0.17
S2	07/10/22 0300	07/10/22 1310	10.2	0.282/0.026	118.4/17	16.6	20.8	1.31/1.54
S3	07/10/22 2215	07/11/22 0608	7.9	0.515/0.06	64.8/18.3	18.2	21.9	0.99/1.00
S4	07/12/22 0600	07/12/22 1007	4.1	0.064/0.005	126.8/25.7	7.6	9.0	2.57/2.57
S5	07/14/22 0828	07/16/22 0830	48	0.637/0.055	156.6/23.1	20.5	25.0	1.11/2.00
S6	07/18/22 0339	07/19/22 1335	33.9	0.474/0.066	93/17.3	27.6	33.1	0.46/0.63
S7	07/21/22 2240	07/22/22 1335	14.9	0.542/0.085	131/41.2	23.3	29.8	0.17/0.07
S8	07/28/22 0015	07/28/22 0653	6.6	0.065/0.006	84/26.6	9.2	12.6	1.00/0.39
S9	07/30/22 0328	07/30/22 1205	8.6	0.321/0.054	66.1/19.4	25.4	30.9	0.37/0.15

Columns are: RVE numbers, starting and ending times, event duration, max/mean of liquid water content (ql), max/mean of the total number of droplets (Nd), effective diameter (ED), mean volume diameter (MVD), and mean/standard deviation Meteorological Optical Range (MOR).
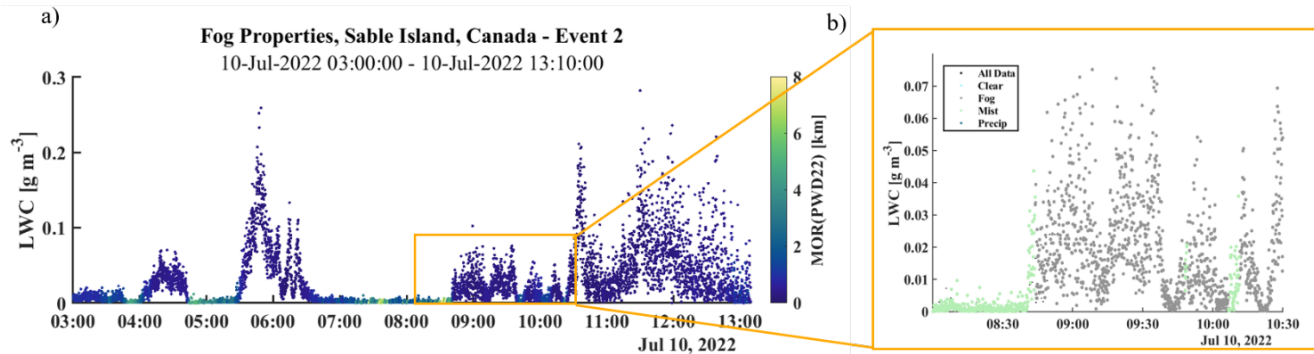

a) Time series of S2 (10-Jul-2022 03:00– 10-Jul 2022 13:10) LWC colored by MOR from the PWD b) zoomed in look of S2 from 10-Jul-2022 08:00 – 10-Jul-2022 10:30) LWC time series categorized by WMO SYNOP code

Figure 6.   Time series of S2

17

B. DROPLET SIZE SPECTRA

Mean droplet size spectra from all the events in Table 1 are shown in Figure 7a. Each spectrum in Figure 7a is obtained by averaging each FM-120 bin over the identified event. The mean spectrum averaged over the entire campaign is also included in Figure 7 (the gray line). The spectra show a bimodal distribution in seven of the nine events and over the full dataset. The local peaks are about 4.4 μm and 25 μm. S4 and S8 have the lowest mean LWC and smallest mean ED; their spectrum diverges from the bimodal distribution starting at a droplet diameter larger than 13.6 μm. Of note, S4 and S8 are the two shortest events, 4.1 and 6.6 hours, respectively. A study by Isaac et al. (2020) characterizing marine fog offshore Newfoundland and Labrador also showed bimodal size distributions but with peaks near 6 and 25–30 μm. They concluded that larger droplet sizes often contain more liquid water content, especially with higher total liquid water contents (Isaac et al. 2020) which we also note. Wang et al. (2021a) also observed that a bimodal distribution of the size spectra frequently occurred in central California (Wang 2021a).
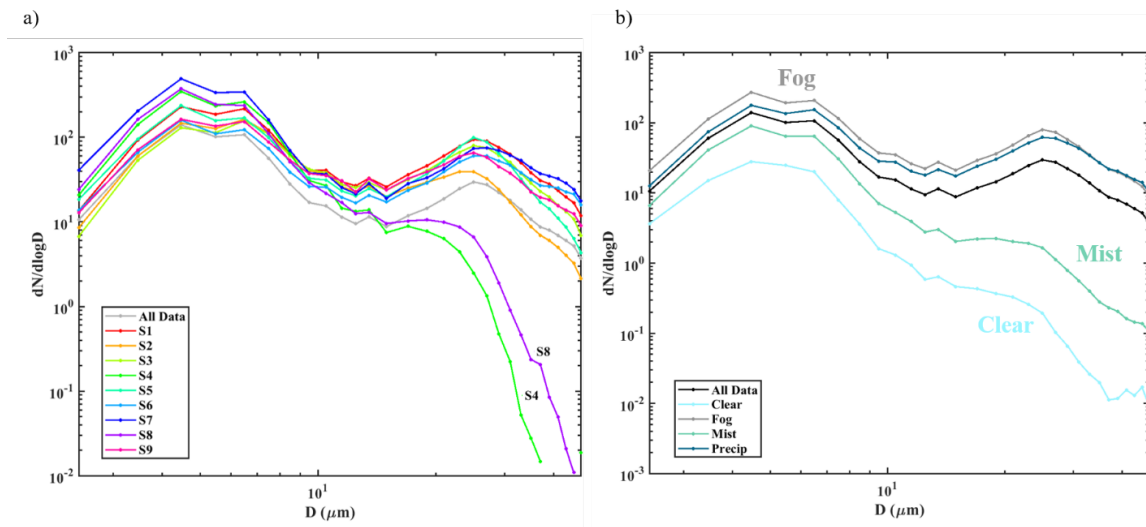
a) Mean droplet size distribution measured by FM-120. The legend corresponds to the events in Table 1. Events S4 and S8 are annotated. b) Mean droplet size distribution measured by the FM-120 and categorized by WMO SYNOP code. WMO SYNOP codes are annotated in the Figure.

Figure 7.   Mean droplet size distribution measured by FM-120

Figure 7b shows the mean droplet size spectra over the full campaign categorized by WMO SYNOP weather code. The FM-120 droplet bin averages were taken over each condition for the complete dataset. The fog and precipitation spectrums seemingly mirror each other, with precipitation showing slightly higher droplet concentration than fog for large droplets. One factor to keep in mind is that the FM-120 maximum droplet size is 50μm. The instrument does not capture the precipitable size droplets beyond the measurable size range. Therefore, the LWC shown here only includes contributions from droplets up to 50μm while the total water in the precipitation events may be higher. Unfortunately, the disdrometer on Sable Island for raindrop spectra malfunctioned during the FATIMA field campaign. We hence do not have the precipitation droplet spectra other than the RAINCAP data indicating the presence of precipitation. The all-data spectrum mirrors the bimodal distribution of the fog and precipitation but to a lower magnitude. The divergence of the mist and clear spectra from the pack generally increases with droplet size. An irregular increase in the clear spectrum is seen in the largest droplets. Note that the weather code was defined based on the PWD22 measured visibility. Because of the temporal variability discussed earlier (Figure 6), the time period identified as 'clear' may contain scattered sections with observable hydrometers, and hence the droplet spectrum during the 'clear' periods in Figure 7b.
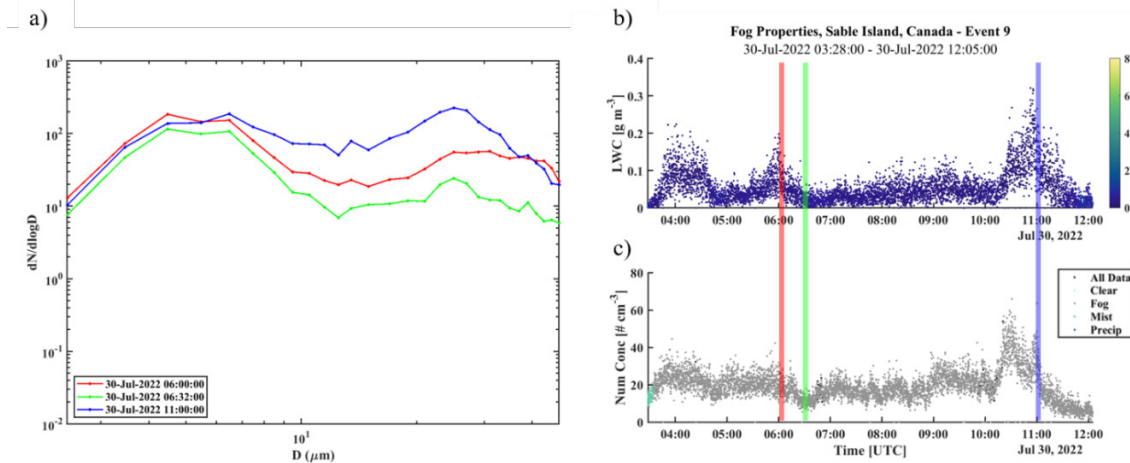
a) Mean droplet size distribution measured by FM-120. Each spectrum was obtained by averaging over 10 minutes plus or minus 5 minutes from the time listed in the legend. b) Time series of S9 (03:28– 12:05 30-Jul 2022) LWC colored by MOR from the PWD. c) Time series of N_d categorized by WMO SYNOP code. The red, green, and blue lines correlate to the mean droplet size distributions in Figure 8a.

Figure 8.   S9 mean droplet size distribution and time series

C.   CASE STUDY ANALYSIS – S9

While there are evident similarities in the mean droplet size spectrum in S1-S3, S5-S7, and S9, the droplet spectra show clear temporal variability. Figure 8 shows an example from S9 using the droplet spectra averaged over three 10 minute sections of the data. The three data sections represent different fog liquid water content under predominantly fog conditions (MOR < 1 km). The highest variability is seen in larger droplets. While 06:00 and 11:00 are both at the peaks of LWC, the corresponding spectra have noteworthy differences in medium and large droplet distribution. N_d at 11:00 is higher than that at 06:00. S9 lasted for 8 hours and 39 minutes that was foggy 99% of the time (Figure 8b).

The temporal variation of the atmospheric conditions during S9 is shown in Figure 9. The radiosonde soundings illustrate the evolution of temperature, relative humidity, wind speed, and wind direction. We can also identify the evolution of the fog layer depth using the individual relative humidity profile from all Sable Island soundings. Figure 9 shows the boundary layer evolution from initially a thick fog layer, up to 0.72 km, to a thinner layer with increasing LWC after 07:00. At the start of the event, the air is dry above 1km, and an upper cloud layer from 1.2-3km is present. Strong wind shear is present, and

20

surface-level winds are from the south-southwest with westerly winds above and winds more southwesterly aloft. As time progressed, the upper air became drier and visibility increased as the surface winds decreased and shift to the southwest. This highlights the spatial variability of fog. With the wind shift, another patch of fog may have entered the observation area.
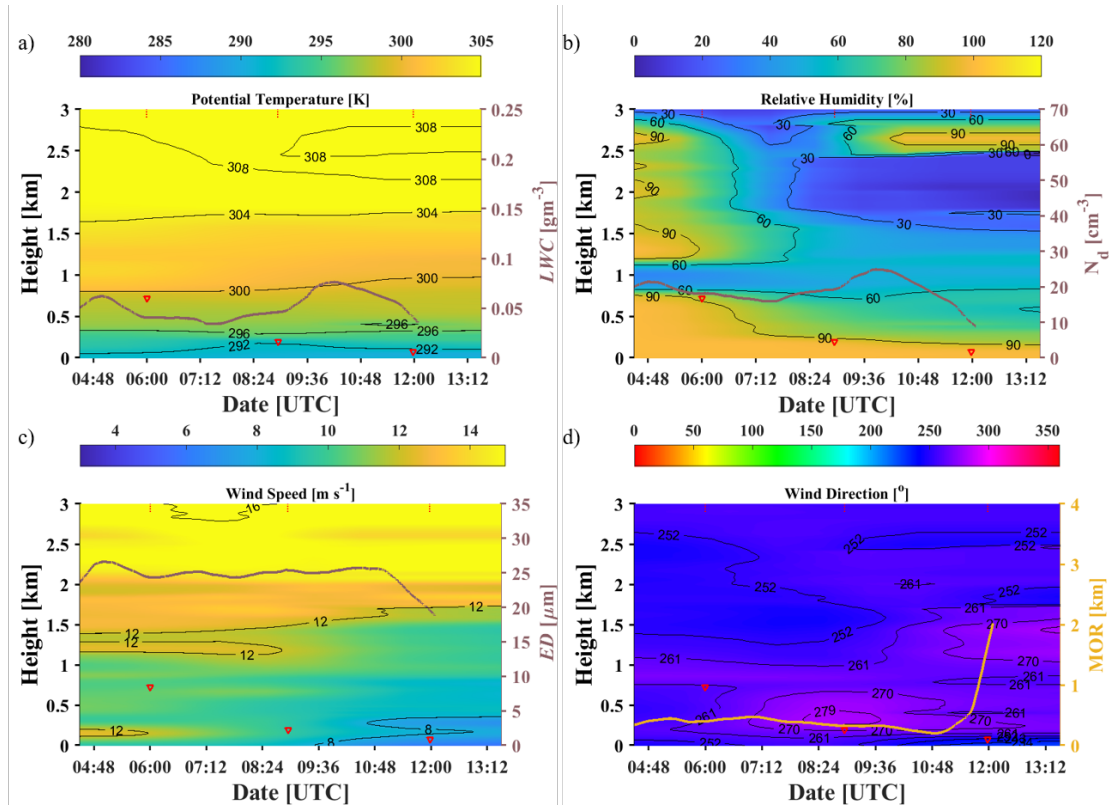

Time-height plots from radiosonde measurements. of a) potential temperature, b) relative humidity, c) wind speed, and d) wind direction. The magenta dotted lines at the top of each subplot delineate the time of each radiosonde launch. The red downward triangles denote the fog layer top, as identified from the analysis of individual soundings. Microphysical properties from the FM-120, LWC, Nd, and ED are shown on the right axes (brown lines on each plot) for subplots a-c. Microphysical properties are 30-min averages. In subplot d, MOR from the PWD22 is shown on the right axis (golden line).

Figure 9.   S9 time-height plots from radiosonde measurements

D.   IMPACTS OF MICROPHYSICS ON VISIBILITY

In this section, we focus on an evaluation of the relationship between LWC and visibility since LWC is the most common output product of fog/cloud in all mesoscale

21

forecast models. Figure 10 shows the temporal variability of LWC and N_d color coded with visibility variation for the entire period. We see that the occurrence of reduced visibility to 1km and below was always related to periods of relatively high LWC and the darkest color (lowest visibility) is associated with the peaks of LWC in all identified RVEs. The periods outside the RVEs when non-zero LWC were observed all have very low liquid water content with peaks far below 0.1 gm^{-3}. The association of periods of reduced visibility to N_d is not as 'clean' as that to LWC (Figure 10b). While in general, significantly reduced visibility was observed during periods of high N_d, larger N_d does not necessarily correlate to low optical range, as seen between 5-9 July, which had to do with the weak correlation between LWC and N_d in periods of low LWC. Events S4 and S8 are examples of periods with high N_d and low LWC. Both events contain a broad range of N_d with large variability in MOR, LWC, N_d, ED, and MVD (Figure 4a, Table 1, and Figure 10). The independence of these variabilities inherently led to more scattering between MOR and N_d.
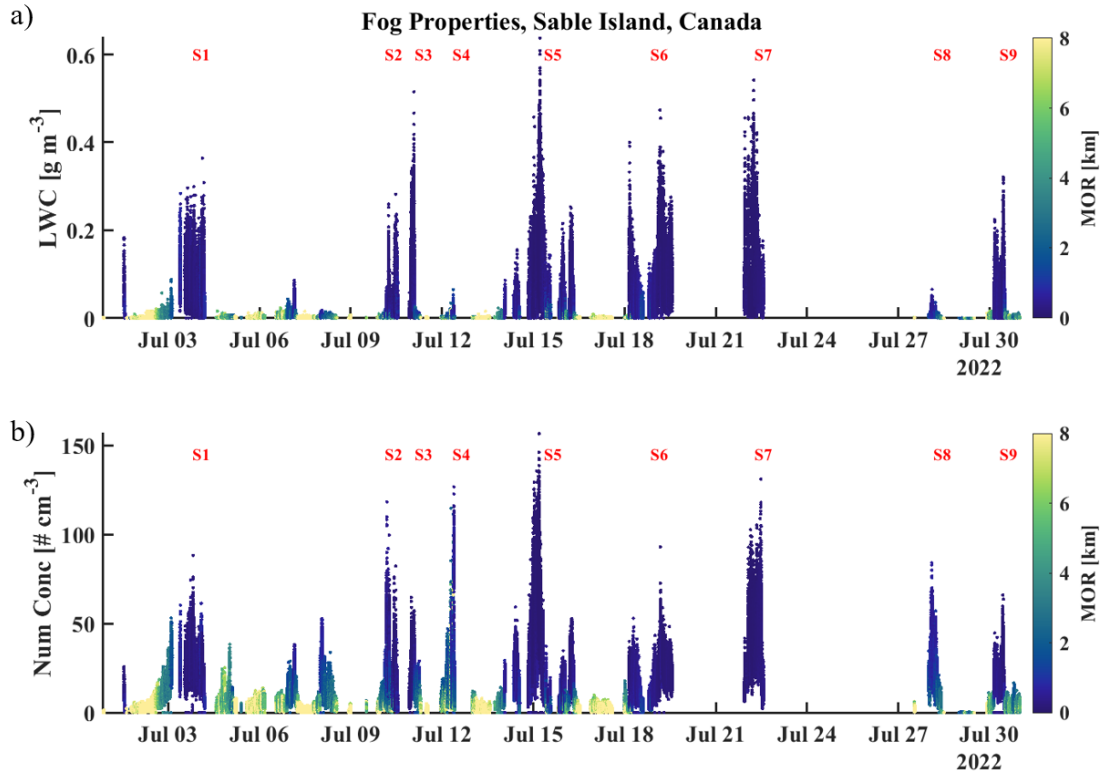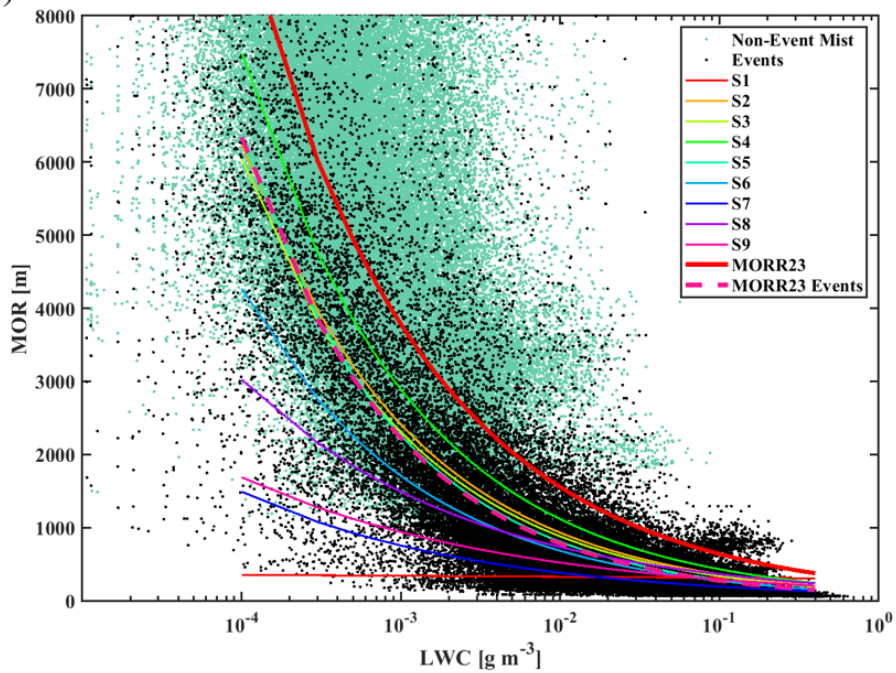
a) Time series of LWC colored by MOR from the PWD. b) Time series of N_d colored by MOR from the PWD. The previously identified RVEs are labeled in red text at the top of each figure.

Figure 10.   Time series of LWC and N_d colored by MOR from the PWD

23
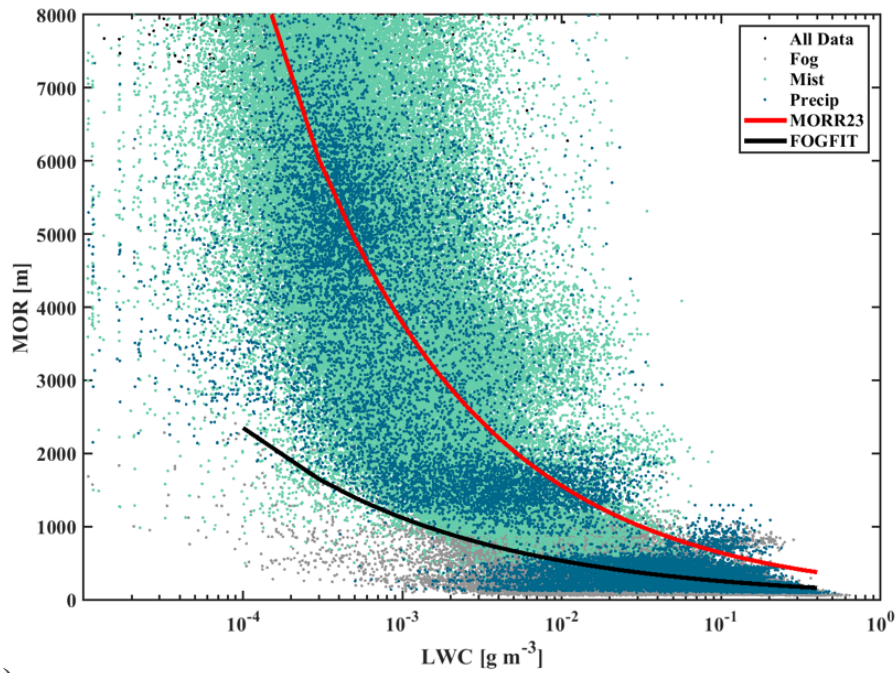
a) Variation of MOR with LWC separated by different weather codes. The red line is the best-fit power relationship using all measured data; b) Same as in (a) except the data are separated by those within the RVESs (black dots) and others (green dots). The dashed magenta line denotes the best fit using all the data within the identified RVEs, the red line is the same as in (a), and the color lines denote the fit for each individual event.

Figure 11.   Variation of MOR with LWC separated by different weather codes

The relationship between MOR and LWC is examined for different conditions. This study evaluated a power relationship between MOR and LWC ($MOR = aq_l{}^b$), where q_l is the LWC in g m^{-3}. The power function form is frequently used in the literature (Wang 2021a; Gultepe et al. 2021; Gultepe 2017). The coefficients, *a* and *b*, are obtained by a least-square fit to the measured data for MOR less than 10km and LWC greater than 10^{-5} g m^{-3}. Therefore, clear conditions are not included in defining the relationships.

Figure 11 shows the relationship between MOR and LWC presented in different ways. In Figure 11a, the different color symbols represent the three weather code conditions. Note that while the 'mist', and 'fog' conditions were identified based solely on the measured visibility, the precipitation conditions are based on the RAINCAP measurements regardless of visibility. Figure 11a shows a general trend of increased MOR with reduced LWC for all weather code cases, although the data points scatter within a wide envelope of both LWC and MOR. We also noticed that the MOR during periods of precipitation follows the same general trend of fog and mist well, although the majority of the precipitation conditions resulted in visibility below 1km. Furthermore, the MOR variability during the identified precipitation periods appears similar to that of fog/mist. Since the LWC here is based on the spectra measurements of the FM-120, it does not include contributions from rain drops with a diameter greater than 50 μm. Results in Figure 11a suggest minimum impact from larger droplets in the light rain conditions.

Figure 11a also shows two fitted lines using a power relationship. The red line is the result of using all the data to include mist, fog, and precipitation conditions, and the black line is the fitted result using the fog conditions only. Although the 'best' fit for the data points, the fitted function for all the data seems to overestimate the measured MOR in the foggy and dense mist (MOR less than 2-3km) conditions and underestimate the measured MOR in the light mist conditions (MOR greater than 5 km). The fitted line for all fog conditions (black) gives a significantly different relationship from the all-data results. However, the results appear to depict the population of fog data much better than the fit using all data points. These results suggest that the simple power function may not be the most appropriate form of relationship to represent the broad range of MOR under fog/mist/precipitation conditions.

25

The MOR-LWC relationship may vary in different ranges of visibility shown in Figure 11b where the data is separated into event (black dots) vs non-event mist conditions (green dots). The event points include all data from the RVEs (S1-S9) and the green dots are from the mist conditions outside the events (Figure 4 and 10). The colored lines are the power law fit for each individual event, while the thick magenta dash and the red lines represent the power law fit for the event-only data and for all data, respectively. The red line in both Figure 11a and b are the same. As discussed earlier, different weather conditions represented by the weather code can be present in an event even though the event mean visibility is less than 1km by definition. Similar to what was observed in Figure 11a, the red line does not fit the combination of the green and black dots (all data) well. In contrast, the power law fit for the RVE works better for the black symbol population, again an indication that the power law fit works better for low visibility cases.

The fitted functions for each event show further MOR-LWC relationship complications. Events 1, 7, and 9 have the lowest observed mean MOR ranging between 0.17 and 0.37km (Table 1). These events also have the least presence of mist which can be identified from the time series plots of the weather code conditions (not shown). Events 7 and 9 are both primarily fog events, they show a similar MOR-LWC relationship, indicating the slowest drop in MOR as LWC increases, mostly in the high LWC/low visibility regime. Event 1 has a mixture of mostly precipitation conditions with short periods of fog. It is the only one out of all nine events that does not show an identifiable relationship between MOR and LWC. We have traced this unclear relationship to possible uncertainties with the FM-120 measurements. The FM-120 housekeeping data for this event indicated sections of bad measurement quality, resulting in the removal of some of the data sections (see discussion in Section 3). It is possible that the remaining data in this event also has a data quality issue, leading to unexpected results. Hence the fitted lines from events 7 and 9 are considered the relationship for very low visibility cases. Figure 11b clearly indicates that the best-fit relationship from these cases cannot be extended to cases with extensive presence of mist (i.e., low LWC regime).

Out of the remaining six events, S2, S3, and S5 have nearly the same best fit curve and are nearly identical to the best for all the event data (magenta dash line and the black

26

dots). These three events also have the most similar droplet size (MVD of 20.8, 21.9, and 25.0 μm for S2, S3, and S5, respectively). Events S4 and S8 are the two weakest events in terms of mean LWC have nearly identical droplet size spectra in the small droplet size range although S8 had slightly larger number of large droplets above 13 μm (Figure 7), resulting in slightly larger mean MVD and ED. The two events also had nearly the same mean total droplet number concentration and LWC. However, their MOR variability with LWC is substantially different (Figure 11b). As an example, for a given fog LWC of 0.01 g m^{-3}, the MOR values from the S4 and S8 fitted relationship are 1.117 and 0.735 km, resulting in a difference of around 382 m. The differences are largely at the small LWC range by nature of the power law fit. Event S8 has a much lower visibility compared to other mixed fog/mist events such as S2, S3, and S5 and compared to S4 with slightly droplet spectra. It is not clear whether the difference can be explained by scattering theory due to the slight difference in their droplet size spectra.

27
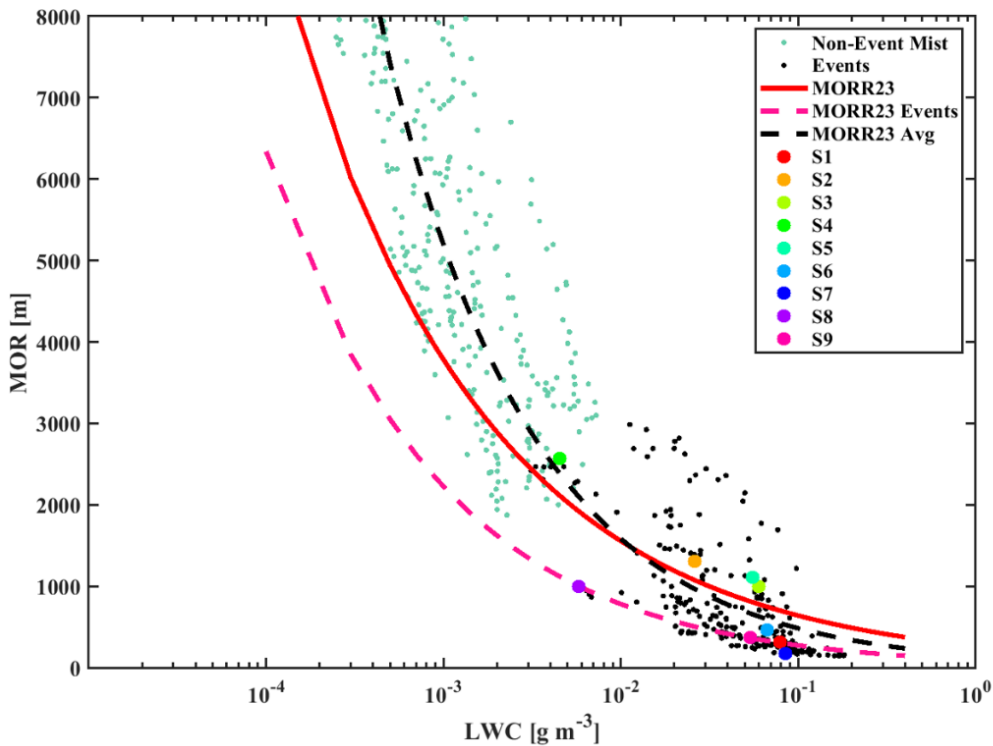
The black dots are the hourly averaged values from the nine selected visibility reduction events. The best fit for the black dots is given in the black dash line (MORR23 Avg) extended to the mist region with low LWC and high MOR. The red (MORR23) and magenta dash (MORR23 Events) lines are the best-fit lines for all 1-min averaged data points as in Figure 11a and the event data in Figure 11b, respectively. The bigger colored dots are the mean event values for S1 to S9.

Figure 12.   MOR variations with LWC for the hourly averaged observational data from Sable Island

The purpose of investigating the MOR-LWC relationship is to better depict visibility based on the forecast LWC in most mesoscale forecast models for improved fog microphysics. However, forecast models have a grid resolution of a nominal kilometer or several kilometers and generally with an hourly or three-hourly output of forecast product, including LWC. Given the variability of both LWC and MOR, it is interesting to examine how the MOR-LWC relationship may vary if longer time-averaged data are used. Figure 12 shows the hourly averaged MOR-LWC scatter plot with the black dot being data from the identified events and the green dots from the non-event mist period. In Figure 12, the MOR-LWC relationship derived from the 1-min event data (magenta dash line) seems to

28

represent the hourly averaged fog event (MOR < 1 km) well but cannot be extended to the mist regime. This outcome is expected based on Figure 11b. However, the best-fit power relationship for the hourly data, *MORR23 Avg,* (black dash) is substantially different from the 1-min fit data, *MORR23 Events,* (magenta dash line). Both fit lines are very different from the red line, the best fit for all 1-min data in Fig. 11a. Because of the large temporal variation of visibility, the hourly average for a case with a mixture of fog and mist may misrepresent both the fog and mist conditions due to the nature of the averaging, which explains that the best fit for the hourly data does not represent the fog conditions well. This situation likely happens in the forecast hourly model output, especially for mixed fog/mist conditions. Representing MOR with the hourly LWC output therefore may have inherent limitations due to its coarse spatial and temporal resolution. The event-averaged data (Table 1) are also shown in Figure 12 as a reference. Here the dense fog cases appeared to be represented well by the fit derived from the 1-min event averaged data, but not so for the high visibility events.

THIS PAGE INTENTIONALLY LEFT BLANK

V. SUMMARY AND CONCLUSION

This study uses the measurements on the upwind side of a small and flat island in the North Atlantic Ocean during the Fatima Grand Banks field campaign in July 2022. The data used in this study were measured by the FM-120 fog spectrometer, a PWD22 present weather sensor with the RAINCAP, and radiosonde launches throughout the measurement period. Data quality for the fog microphysics data was made by eliminating sections of bad data indicated by the FM-120 housekeeping records.

The radiosonde measurements made multiple times each day revealed the general thermodynamics structure and its temporal variations over Sable Island. The lower atmosphere was characterized by a shallow boundary layer frequently in weak stable stratification and with fog layers ranging from tens of meters to several hundred meters in depth. The most prominent feature of the Sable Island boundary layer during the measurement period is the frequent occurrence of high wind conditions with a low-level jet with the presence of fog. The jet can be completely immersed inside the fog layer or with the peak wind level above the fog layer, resulting in substantial vertical wind shear within the fog layer. The maximum observed surface wind is close to 16 ms^{-1}.

The month of July saw frequent occurrence of fog which was expected based on the local climatology. The maximum fog LWC can reach as high as 0.64 gm^{-3}, with the maximum number concentration reaching 157 cm^{-3} and the mean droplet concentration ranging between 17 and 27 cm^{-3}. For most of the fog events, the effective diameter varied between 16 and 28 μm, with two cases of smaller droplet size averaging at 7.6 and 9.2 μm. Based on the measured visibility and the presence of precipitation, the entire measurement period is categorized into four weather code conditions including 'clear', 'mist', 'fog', and 'precipitation' conditions. Mist is the most frequently observed condition (41%) followed by fog (35%). Precipitation happened about 13% of the time during the measurement period.

Based on the mean visibility, we identified 9 reduced visibility events (RVEs) to focus on their microphysics characteristics. Because of the large variability in visibility and

31

precipitation, the identified RVEs are mostly mixtures of fog, mist, and precipitation conditions. With the exception of two events (S4 and S8), seven events show the bimodal distribution in droplet spectra with the lower peak at 4-5 um and the higher peak at 25-30 μm. Interestingly, when the droplet spectra are examined based on the weather code, we found fog and precipitation conditions have nearly identical shapes of droplet spectra except that slightly more number concentrations are found in the fog condition compared to precipitation conditions within the size range of $2 - 50$ μm limited by the upper size boundary of the FM-120. Mist, on the other hand, mainly consists of small droplets with similar size distribution as fog below around 13 μm except with a smaller number concentration. Some droplets were also in the 'clear' conditions as the category was defined based on visibility greater than 10 km. However, we also identified strong temporal variability in the droplet spectra with most of the variations seen in the large droplet size range above 10 μm (Figure 8). An example of the temporal evolution of the fog layer suggests the corresponding evolution of the wind and thermodynamic conditions above the fog layer. It is possible what appeared to be the temporal variability is essentially a result of spatial variability upwind of Sable Island and the gradually thinning fog layer may be associate with entrainment drying when the shallow boundary layer mixed with the dry air from the inversion.

A detailed investigation of the dependence of MOR on liquid water content reveals the limitation of using a single power law function to represent both the fog and mist regimes. While the power function traditionally used in the literature may work well for moderate fog with mist for certain events, there is no universal relationship that can be used to describe the MOR-LWC dependence as the dense fog and light fog/mist may be represented by very different power functions. A more sophisticated fit function is likely needed, although we were not able to identify such a function given the limited cases we have found.

LIST OF REFERENCES

Albrecht, B.A., 1989: Aerosols, cloud microphysics, and fractional cloudiness. *Science*, **245**(4923), 1227–1230, https://doi.org/10.1126/science.245.4923.1227.

Bergot, T., 2013: Small-scale structure of radiation fog: A large-eddy simulation study. *Q. J. Roy. Meteor. Soc.*, **139**, 1099–1112.

Correia, A. L., M. M. Mendonça, T. F. Nobrega, A. C. Pugliesi, and M. A. Cecchini, 2022: A multi-year study of GOES-13 droplet effective radius retrievals for warm clouds over South America and Southeast Pacific. *Atmosphere*, **13**, 77, https://doi.org/10.3390/atmos13010077.

Dorman, C.E., 2017: Worldwide marine fog occurrence and climatology. *Marine fog challenges and advancements in observations modeling and forecasting*, D. Koračin, C.E. Dorman, Eds., Springer, 153–158.

Droplet Measurement Technologies, 2018: *Fog Monitor Model FM-120 Operator Manual,* DOC-0339 Revision B-1. Longmont, Colorado.

Dupont, J. C., M. Haeffelin, S. Stolaki, and T. Elias, 2016: Analysis of dynamical and thermal processes driving fog and quasi-fog life cycles using the 2010–2013 ParisFog dataset. *Pure Appl. Geophys.*, **173**, 1337–1358.

Fernando, H. J. S., and Coauthors, 2021: C-FOG: Life of coastal fog. *Bull. Amer. Meteor. Soc.*, **102**(2), E244–E272, https://doi.org/10.1175/BAMS-D-19-0070.1.

Fuzzi, S. and Coauthors, 1992: The Po Valley fog experiment 1989. *Tellus B*, **44**, 448–468, https://doi.org/10.1034/j.1600-0889.1992.t01-4-00002.x.

Garcia-Garcia, F., U. Virafuentes, and G. Montero-Martinez, 2002: Fine-scale measurements of fog-droplet concentrations: a preliminary assessment. *Atmos. Res.,* **64**, 179–189, https://doi.org/10.1016/S0169-8095(02)00075-6.

Gerber, H. E., 1981: Microstructure of a radiation fog. *J. Atmos. Sci.*, **38**, 454–458, https://doi.org/10.1175/1520-0469(1981)038<0454:MOARF>2.0.CO;2.

Gerber, H. E., 1991: Supersaturation and droplet spectral evolution in fog. *J. Atmos. Sci.*, **48**, 2569–2588, https://doi.org/10.1175/15200469(1991)048<2569:SADSEI>2.0.CO;2.

Gultepe, I., 2017: Worldwide marine fog occurrence and climatology. *Marine fog challenges and advancements in observations modeling and forecasting*. D. Koračin, C.E. Dorman, Eds., Springer, 345-370.

Gultepe, I., and Coauthors, 2007: Fog research: A review of past achievements and future perspectives. *Pure Appl. Geophys*., **164**, 1121–1159.

Gultepe, I., and Coauthors, 2021: A Review of Coastal Fog Microphysics During C-FOG. *Boundary-Layer Meteorology,* **181**, 227–265, https://doi.org/10.1007/s10546-021-00659-5.

Gultepe, I., M. D. Müller, and Z. Boybeyi, 2006: A new visibility parameterization for warm-fog applications in numerical weather prediction models. *J. Appl. Meteor. Climatol.*, **45**, 1469–1480, https://doi.org/10.2307/26171867.

Isaac, G. A., T. Bullock, J. Beale, and S. Beale, 2020: Characterizing and Predicting Marine Fog Offshore Newfoundland and Labrador. *Weather and Forecasting*, **35**(2), 347-365. https://doi.org/10.1175/WAF-D-19-0085.1.

Jiusto, J. E., 1981: Fog structure. *Clouds: Their Formation, Optical Properties and Effects*, P. V. Hobbs and A. Deepak, Eds., Academic Press, 495 pp.

King, W. D., D. A. Parkin, and R. J. Handsworth, 1978: A hot-wire liquid water device having fully calculable response characteristics. *J. Appl. Meteor.*,**17**(12), 1809–1813, https://doi.org/10.1175/1520-0450(1978)017<1809:AHWLWD>2.0.CO;2.

Koračin, D., J. Lewis, W. T. Thompson, C. E. Dorman, and J. A. Businger, 2001: Transition of stratus into fog along the California coast: Observations and modeling. *J. Atmos. Sci.*, **58**, 1714–1731. https://doi.org/10.1175/1520-0469(2001)058<1714:TOSIFA>2.0.CO;2.

Mazoyer, M., F. Burnet, C. Denjean, G. C. Roberts, M. Haeffelin, J. C. Dupont, and T. Elias, 2019: Experimental study of the aerosol impact on fog microphysics, *Atmos. Chem. Phys.*, **19**, 4323–4344, https://doi.org/10.5194/acp-19-4323-2019.

Morrison, H., and Coauthors, 2020: Confronting the challenge of modeling cloud and precipitation microphysics. *J. Adv. Model. Earth Syst*., **12**, e2019MS001689, https://doi.org/10.1029/2019MS001689.

Petty, G.W., 2004: *A first course in atmospheric radiation.* Sundog Publishing, 472 pp.

Price, J.D., 2019: On the formation and development of radiation fog: An observational study. *Boundary-Layer Meteorol.,* **172**, 167–197, https://doi.org/10.1007/s10546-019-00444-5.

Roach, W. T., 1976: On the effect of radiative exchange on the growth by condensation of a cloud or fog droplet. *Q. J. R. Meteorol. Soc.,* **102**, 361–372, https://doi.org/10.1002/qj.49710243208.

Stoelinga, M. T., and T. T. Warner, 1999: Nonhydrostatic, mesobeta-scale model simulations of cloud ceiling and visibility for an east coast winter precipitation event. *J. Appl. Meteor.*, **38**(4), 385–404.

Twomey, S., 1977: The influence of pollution on the shortwave albedo of clouds. *J. Atmos. Sci.*, **34**(7), 1149–1152. https://doi.org/10.1175/1520-0469(1977)034<1149:TIOPOT>2.0.CO;2.

Vaisala, 2004: *Present Weather Detector PWD22 User's Guide*, M210543EN-B. Helsinki, Finland.

Wang, Q., and B. A. Albrecht, 1994: Observations of Cloud-Top Entrainment in Marine Stratocumulus Clouds. *J. Atmos. Sci*., **51**, 1530–1547, https://doi.org/10.1175/1520-0469(1994)051<1530:OOCTEI>2.0.CO;2.

Wang, Q., and Coauthors, 2021a: Microphysics and Optical attenuation in fog: observations from two coastal sites. *Boundary-Layer Meteorology,* **181**, 267–292, https://doi.org/10.1007/s10546-021-00675-5.

Wang, S., H. J. S. Fernando, C. Dorman, E. Creegan, R. Krishnamurthy, C. Wainwright, S. Wagh, and R. Yamaguchi, 2021b: Analysis of coastal fog from a ship during the C-FOG campaign. *Boundary-Layer Meteorology*, **181**, 365–393 (2021). https://doi.org/10.1007/s10546-021-00667-5.

THIS PAGE INTENTIONALLY LEFT BLANK

INITIAL DISTRIBUTION LIST

1.   Defense Technical Information Center
        Ft. Belvoir, Virginia

2.   Dudley Knox Library
        Naval Postgraduate School
        Monterey, California